

# DTR: A Unified Deep Tensor Representation Framework for Multimedia Data Recovery

Ting-Wei Zhou, Xi-Le Zhao\*, Jian-Li Wang, Yi-Si Luo, Min Wang, Xiao-Xuan Bai,  
and Hong Yan

**Abstract**—Recently, the transform-based tensor representation has attracted increasing attention in multimedia data (e.g., images and videos) recovery problems, which consists of two indispensable components, i.e., transform and characterization. Previously, the development of transform-based tensor representation mainly focuses on the transform aspect. Although several attempts consider using shallow matrix factorization (e.g., singular value decomposition and negative matrix factorization) to characterize the frontal slices of transformed tensor (termed as latent tensor), the faithful characterization aspect is underexplored. To address this issue, we propose a unified Deep Tensor Representation (termed as DTR) framework by synergistically combining the deep latent generative module and the deep transform module. Especially, the deep latent generative module can faithfully generate the latent tensor as compared with shallow matrix factorization. The new DTR framework not only allows us to better understand the classic shallow representations, but also leads us to explore new representation. To examine the representation ability of the proposed DTR, we consider the representative multi-dimensional data recovery task and suggest an unsupervised DTR-based multi-dimensional data recovery model. Extensive experiments demonstrate that DTR achieves superior performance compared to state-of-the-art methods in both quantitative and qualitative aspects, especially for fine details recovery.

**Index Terms**—Deep tensor representation, deep latent generative module, deep transform module, multi-dimensional data recovery.

## I. INTRODUCTION

MULTIMEDIA data, such as color images [1]–[3], multispectral images (MSIs) [4], [5], magnetic resonance imaging (MRI) images [6], and videos [7], [8], is commonly encountered in various real-world applications, including but not limited to agricultural monitoring [9], hyperspectral image (HSI) restoration [10], [11], and medical imaging [12].

Ting-Wei Zhou and Xi-Le Zhao are with the School of Mathematical Sciences/Research Center for Image and Vision Computing, University of Electronic Science and Technology of China, Chengdu, Sichuan 611731, China (e-mail: zhoutingwei2021@163.com; xlzhao122003@163.com).

Jian-Li Wang is with the School of Computing and Artificial Intelligence, Southwest Jiaotong University, Chengdu, Sichuan 611756, China (e-mail: wangjianli\_123@163.com).

Yi-Si Luo is with the School of Mathematics and Statistics, Xi'an Jiaotong University, Xi'an 710049, China (e-mail: yisiluo1221@foxmail.com).

Min Wang is with the School of Information Management, Jiangxi University of Finance and Economics, Nanchang, Jiangxi 330013, China (e-mail: minwang1989@126.com).

Xiao-Xuan Bai is with the Glasgow College, University of Electronic Science and Technology of China, Chengdu, Sichuan 611731, China (e-mail: abnxxa@outlook.com).

Hong Yan is with the Department of Electrical Engineering, City University of Hong Kong, Kowloon, Hong Kong SAR (e-mail: h.yan@cityu.edu.hk).

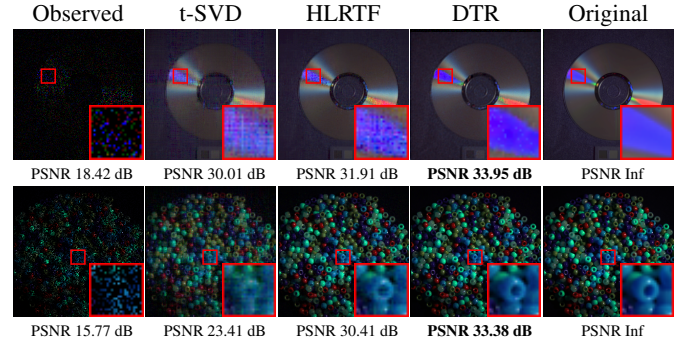


Fig. 1: The recovered pseudo-color images (R:10, G:20, B:30) by shallow characterization-based methods, i.e., t-SVD (based on SVD) [16] and HLRTF (based on negative matrix factorization) [17], and deep characterization-based method, i.e., the proposed DTR.

However, the acquired multimedia data is usually incomplete owing to sensor failures or other abnormal conditions that occur during the acquisition and transmission process, which can severely hinder subsequent applications [13]–[15]. The task of estimating missing data from the observed data can be formulated as the multimedia data recovery problem. Besides, with the development of multimedia technology, multimedia data has become increasingly multi-dimensional. Hence, it is important to develop effective multi-dimensional data recovery methods.

Recently, the transform-based tensor representation has emerged as a powerful tool for multi-dimensional data recovery problems, as demonstrated by extensive studies [17]–[22]. The transform-based tensor representation represents the multi-dimensional data as an implicit low-rank tensor and exploits its low-rankness in the transform domain. In the transform-based tensor representation, two indispensable components are (i) the transform that captures the frontal slice relationships of multi-dimensional data [20]–[22], and (ii) the characterization of the frontal slices of transformed tensor (termed as latent tensor) [23]–[25].

Previously, the development of transform-based tensor representation mainly focuses on the transform perspective, such as the discrete Fourier transform (DFT) [23], [26], the discrete cosine transform (DCT) [22], unitary transform [27], [28], non-invertible transform [20], [29], [30], and nonlinear transform [17]. However, few methods have paid attention to the second component, i.e., the characterization of the frontal

slices of latent tensor. To date, the transform-based tensor representation usually adopts shallow matrix factorization to characterize the frontal slices of latent tensor, such as singular value decomposition (SVD) [23], negative matrix factorization (NMF) [17], [24], and QR decomposition [25], [31]. Due to the limited characterization ability, these shallow methods may not be expressive enough to faithfully characterize the latent tensor. Moreover, shallow matrix factorization characterizes the intra-slice relationships of latent tensor separately, which neglects the inter-slice relationships of latent tensor.

To address the above issues, we propose a unified **Deep Tensor Representation** (termed as DTR) framework by synergistically combining the deep latent generative module and the deep transform module. Specifically, we suggest a deep latent generative module to faithfully generate the latent tensor by characterizing both intra-slice and inter-slice relationships of latent tensor. Meanwhile, we utilize an untrained neural network applied on the third dimension of latent tensor as the deep transform module to capture the frontal slice relationships of multi-dimensional data. The new DTR framework not only allows us to better understand the classic shallow representations, but also leads us to explore new representation. To examine the representation ability of the proposed DTR, we consider the representative multi-dimensional data recovery task and suggest an unsupervised DTR-based multi-dimensional data recovery model. Thanks to the superior characterization ability of deep latent generator, our method can obtain better multi-dimensional data recovery results than shallow characterization-based methods; as shown in Fig. 1.

The main contributions of this study are:

- To overcome the limitations of shallow characterization in the transform-based tensor representation, we propose a unified deep tensor representation framework, i.e., DTR, by synergistically combining the deep latent generative module and the deep transform module. The new DTR framework not only allows us to better understand the classic shallow representations, but also leads us to explore new representation.
- Based on the DTR, we propose an unsupervised multi-dimensional data recovery model. Experimental results demonstrate that the proposed method can achieve significant performance improvements over state-of-the-art methods, especially for fine details recovery.

This paper is organized as follows. Section II introduces necessary notations and preliminaries. Section III provides a review of related work. Section IV presents the proposed DTR. Section V and VI present the results of extensive experiments and discussions. Finally, we conclude this work in Section VII.

## II. NOTATIONS AND PRELIMINARIES

### A. Notations

Matrices and tensors are denoted by capitalized letters, e.g.,  $\mathbf{X}$  and capitalized calligraphic letters, e.g.,  $\mathcal{X}$ , respectively. For a matrix  $\mathbf{X} \in \mathbb{R}^{n_1 \times n_2}$ , we use  $\mathbf{X}(i, j)$  to denote the  $(i, j)$ -th element of  $\mathbf{X}$ . Meanwhile, for a third-order tensor

$\mathcal{X} \in \mathbb{R}^{n_1 \times n_2 \times n_3}$ , we use  $\mathcal{X}(i, j, k)$  to denote the  $(i, j, k)$ -th element of  $\mathcal{X}$ .  $\mathcal{X}^{(k)} \in \mathbb{R}^{n_1 \times n_2}$  denotes the  $k$ -th frontal slice of  $\mathcal{X}$ .  $\odot$  denotes the point-wise multiplication (i.e., Hadamard product). The Frobenius norm of tensor  $\mathcal{X}$  is defined as  $\|\mathcal{X}\|_F = \sqrt{\sum_{i,j,k} |\mathcal{X}(i, j, k)|^2}$ .  $\Delta$  denotes the face-wise product between two tensors [32]. Given  $\mathcal{X} \in \mathbb{R}^{n_1 \times n_2 \times n_3}$ ,  $\mathcal{Y} \in \mathbb{R}^{n_2 \times n_4 \times n_3}$ , the face-wise product between  $\mathcal{X}$  and  $\mathcal{Y}$  is  $\mathcal{X}\Delta\mathcal{Y} = \mathcal{Z} \in \mathbb{R}^{n_1 \times n_4 \times n_3}$ , where  $\mathcal{Z}^{(k)} = \mathcal{X}^{(k)}\mathcal{Y}^{(k)}$  ( $k = 1, \dots, n_3$ ).

### B. Preliminaries

**Definition 1** (Mode-3 Unfolding [33]). *For a third-order tensor  $\mathcal{A} \in \mathbb{R}^{n_1 \times n_2 \times n_3}$ , its mode-3 unfolding  $\mathcal{A}_{(3)}$  is a  $n_3 \times n_1 n_2$  matrix, which satisfies that  $\mathcal{A}_{(3)}(i_3, j) = \mathcal{A}(i_1, i_2, i_3)$ , where  $j = 1 + \sum_{s=1}^2 (i_s - 1)J_s$  with  $J_s = \prod_{m=1}^{s-1} n_m$ .*

**Definition 2** (Mode-3 Tensor-Matrix Product [33]). *The mode-3 tensor-matrix product of a  $n_1 \times n_2 \times n_3$  tensor  $\mathcal{X}$  and a  $J \times n_3$  matrix  $\mathbf{A}$  is a  $n_1 \times n_2 \times J$  tensor denoted by  $\mathcal{X} \times_3 \mathbf{A}$  and satisfied*

$$(\mathcal{X} \times_3 \mathbf{A})(i_1, i_2, j) = \sum_{i_3=1}^{n_3} \mathcal{X}(i_1, i_2, i_3) \mathbf{A}(j, i_3). \quad (1)$$

According to above mentioned two definitions, we have

$$\mathcal{Y} = \mathcal{X} \times_3 \mathbf{A} \Leftrightarrow \mathcal{Y}_{(3)} = \mathbf{A} \mathcal{X}_{(3)}. \quad (2)$$

**Definition 3** (Tensor Tubal-Rank [32]). *The tensor tubal-rank of  $\mathcal{A} \in \mathbb{R}^{n_1 \times n_2 \times n_3}$  is defined as*

$$\text{rank}_t(\mathcal{A}) \triangleq \max_{k=1,2,\dots,n_3} \text{rank} \left( (\mathcal{A} \times_3 \mathbf{F})^{(k)} \right), \quad (3)$$

where  $\mathbf{F} \in \mathbb{R}^{n_3 \times n_3}$  is the DFT matrix.

**Definition 4** (T-Product [32]). *The tensor-tensor product between  $\mathcal{A} \in \mathbb{R}^{n_1 \times n_2 \times n_3}$ , and  $\mathcal{B} \in \mathbb{R}^{n_2 \times n_4 \times n_3}$  is defined as  $\mathcal{A} * \mathcal{B} = ((\mathcal{A} \times_3 \mathbf{F}) \Delta (\mathcal{B} \times_3 \mathbf{F})) \times_3 \mathbf{F}^{-1} \in \mathbb{R}^{n_1 \times n_4 \times n_3}$ , where  $\mathbf{F} \in \mathbb{R}^{n_3 \times n_3}$  is the DFT matrix, and  $\mathbf{F}^{-1}$  is the inverse DFT matrix.*

## III. RELATED WORK

In this section, we briefly review the transform-based tensor representation, with a focus on the advances of two indispensable components, i.e., transform and characterization.

### A. The Transform Perspective

An indispensable component in the transform-based tensor representation is the transform that captures the frontal slice relationships of multi-dimensional data. Over the past decade, researchers have explored various transforms [17], [20], [22], [28], [30] to facilitate the most classic transform-based tensor representation, i.e., tensor singular value decomposition (t-SVD). For instance, Kilmer *et al.* [23] first introduced the DFT along the third dimension under the t-SVD framework. Madathil *et al.* [22] adopted the real-valued DCT to avoid the high computational cost caused by complex operations in DFT-based original t-SVD. Lu *et al.* [21] deduced the new tensor

tubal rank based on the invertible linear transform and provided the theoretical bound for the exact recovery under certain tensor incoherence conditions for tensor completion. Unlike previous invertible transforms, Jiang *et al.* [20] employed the non-invertible framelet transform to construct a framelet latent tensor. In addition to the previously pre-defined transforms, some data-driven transforms have emerged promising results in multi-dimensional data recovery problems. For example, Song *et al.* [28] constructed a data-dependent unitary transform, which can be obtained by taking the SVD of the unfolding matrix. Kong *et al.* [30] defined the new tensor Q-rank based on novel data-dependent transform, which can be learned by principal component analysis. Luo *et al.* [34] proposed a nonlinear transform-based tensor nuclear norm (TNN), where the nonlinear transform is obtained by learning a multi-layer neural network solely using the observed tensor in a self-supervised manner.

### B. The Characterization Perspective

Another indispensable component in the transform-based tensor representation is the characterization of the frontal slices of latent tensor. The original t-SVD [23] adopted the standard matrix SVD to characterize the frontal slices of latent tensor. Zhou *et al.* [24] introduced NMF as an alternative approach to efficiently characterize the low-rankness of the frontal slices of latent tensor. In addition, to further enhance the accuracy and efficiency of the characterization, later work [25], [31] adopted an approximate SVD method based on QR decomposition to characterize the frontal slices of latent tensor, which not only reduces the computational complexity but also yields superior results compared to SVD-based method [16]. Despite the benefits of shallow matrix factorization (such as SVD, NMF, and QR decomposition), they may not be representative enough to characterize the latent tensor. Moreover, shallow matrix factorization characterizes the intra-slice relationships of latent tensor separately, which neglects the inter-slice relationships of latent tensor.

## IV. PROPOSED METHOD

In this section, we first introduce the proposed unified deep tensor representation framework, i.e., DTR. Then, we discuss the relationships between the proposed DTR and classic shallow representations. Finally, we give the unsupervised DTR-based multi-dimensional data recovery model.

### A. The Proposed DTR

Inspired by the transform-based tensor representation, we propose a unified deep tensor representation framework, i.e., DTR, by synergistically combining the deep latent generative module and the deep transform module. The diagram of our DTR framework is shown in Fig. 2, and the mathematical formulation can be expressed as follows:

$$\mathcal{X} = f_{\xi} \circ g_{\theta}(\mathcal{Z}), \quad (4)$$

where  $g_{\theta}(\cdot)$  is the deep latent generative module,  $\theta$  denotes the network parameter of  $g(\cdot)$ , and  $\mathcal{Z}$  is a random noise.  $f_{\xi}(\cdot)$  is

the deep transform module,  $\xi$  denotes the network parameter of  $f(\cdot)$ ,  $\circ$  denotes the composition of functions, and  $\mathcal{X} \in \mathbb{R}^{n_1 \times n_2 \times n_3}$  is the multi-dimensional data represented by the proposed DTR. Two indispensable components in the proposed DTR framework, i.e., the deep latent generative module  $g_{\theta}(\cdot)$  and the deep transform module  $f_{\xi}(\cdot)$ , complement to each other and work together to make up a unified framework. Now, we detailedly introduce the two indispensable components in our DTR framework.

1) *Deep Latent Generative Module*: Previous representation usually adopts shallow matrix factorization to characterize the intra-slice relationships of latent tensor separately, which neglects the inter-slice relationships of latent tensor. In our DTR framework, we suggest the deep latent generative module  $g_{\theta}(\cdot)$  to generate the latent tensor, which can be formulated as follows:

$$\hat{\mathcal{X}} = g_{\theta}(\mathcal{Z}), \quad (5)$$

where  $g_{\theta}(\cdot): \mathbb{R}^{n_1 \times n_2 \times \hat{n}_3} \rightarrow \mathbb{R}^{n_1 \times n_2 \times \hat{n}_3}$ ,  $\theta$  denotes the network parameter of  $g(\cdot)$ ,  $\mathcal{Z} \in \mathbb{R}^{n_1 \times n_2 \times \hat{n}_3}$  is a random noise, and  $\hat{\mathcal{X}} \in \mathbb{R}^{n_1 \times n_2 \times \hat{n}_3}$  represents the latent tensor. Here,  $g_{\theta}(\cdot)$  refers to an untrained neural network that maps a random noise into the latent tensor.

Compared with shallow matrix factorization (e.g., SVD and NMF), the deep latent generator can faithfully generate the latent tensor due to the strong representation ability of untrained neural network. In addition, the deep latent generator can faithfully characterize both intra-slice and inter-slice relationships of latent tensor. Based on these two advantages, the deep latent generator has superior characterization ability than shallow matrix factorization, rationally leading to better performance for recovering the fine details of multi-dimensional data (see examples in Fig. 1).

2) *Deep Transform Module*: Now, we are at the position to generate the multi-dimensional data from the latent tensor. To better capture the frontal slice relationships of multi-dimensional data, we utilize an untrained neural network  $f_{\xi}(\cdot)$  applied on the third dimension of latent tensor as the deep transform module, i.e.,

$$\mathcal{X} = f_{\xi}(\hat{\mathcal{X}}), \quad (6)$$

where  $f_{\xi}(\cdot): \mathbb{R}^{n_1 \times n_2 \times \hat{n}_3} \rightarrow \mathbb{R}^{n_1 \times n_2 \times n_3}$ ,  $\xi$  denotes the network parameter of  $f(\cdot)$ ,  $\hat{\mathcal{X}} \in \mathbb{R}^{n_1 \times n_2 \times \hat{n}_3}$  is the output of  $g_{\theta}(\mathcal{Z})$ , i.e., the latent tensor, and  $\mathcal{X} \in \mathbb{R}^{n_1 \times n_2 \times n_3}$  is the multi-dimensional data represented by the proposed DTR. Here,  $f_{\xi}(\cdot)$  maps the latent tensor into the original domain to capture the frontal slice relationships of multi-dimensional data.

The proposed DTR framework allows us to more deeply understand existing representations. Now, we discuss the relationships between the proposed DTR and classic shallow representations.

**Remark 1.** Let  $\{\mathcal{W}_m \in \mathbb{R}^{r_m \times r_{m-1} \times n_3}\}_{m=1}^L$  (with  $r_L = n_1$ ,  $r_0 = n_2$ ). Suppose that  $g_{\theta}(\cdot)$  is given as follows:

$$g_{\theta}(\mathcal{Z}) = \mathcal{W}_L \Delta \sigma(\mathcal{W}_{L-1} \Delta \cdots \mathcal{W}_3 \Delta \sigma(\mathcal{W}_2 \Delta \mathcal{W}_1 \Delta \mathcal{Z})), \quad (7)$$

where each frontal slice of  $\mathcal{Z}$  is set as an identity matrix,  $\Delta$  denotes the face-wise product between two tensors [32], and

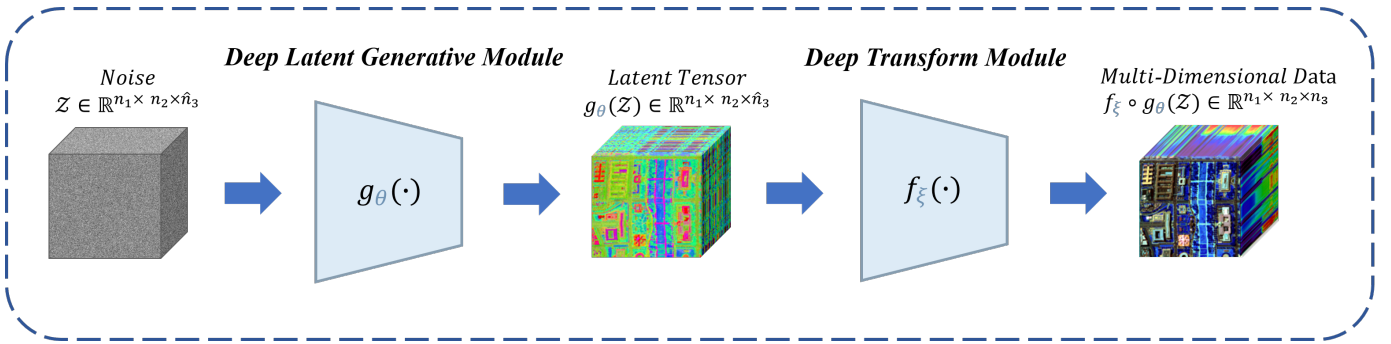


Fig. 2: Diagram of our DTR framework<sup>1</sup>. The deep latent generative module  $g_\theta(\cdot)$  generates the latent tensor and the deep transform module  $f_\xi(\cdot)$  captures the frontal slice relationships of multi-dimensional data.

$\sigma(\cdot)$  is a nonlinear activation function. The proposed DTR can degenerate into classic shallow representations:

- (i) When  $L > 2$  and  $f_\xi(\cdot)$  is set as a identity mapping, our DTR degenerates into the deep matrix factorization [35], [36], which is applied on each frontal slice of the tensor separately.
- (ii) When  $L = 2$  and  $f_\xi(\cdot)$  is set as a deep fully connected network (FCN), our DTR degenerates into the hierarchical low-rank tensor factorization [17].
- (iii) When  $L = 2$  and  $f_\xi(\cdot)$  is set as an inverse DFT, our DTR degenerates into the classic low-tubal-rank tensor factorization [24].

Moreover, the proposed DTR framework also allows us to explore new representation. Previously, the faithful characterization aspect is underexplored. Several attempts consider using shallow matrix factorization (e.g., SVD and NMF) in the transform-based tensor representation to characterize the intra-slice relationships of latent tensor separately, which neglects the inter-slice relationships of latent tensor. To faithfully characterize both intra-slice and inter-slice relationships of latent tensor, we can generate the latent tensor with an untrained neural network by leveraging its expressive power under the DTR framework; see Fig. 1 for the comparison between shallow characterizations and deep characterization in the DTR.

### B. Unsupervised Multi-Dimensional Data Recovery Model

To examine the representation ability of the proposed DTR, we consider the representative multi-dimensional data recovery task and suggest an unsupervised DTR-based multi-dimensional data recovery model, as follow:

$$\min_{\xi, \theta} \|\mathcal{M} \odot (\mathcal{X} - \mathcal{O})\|_F^2, \text{ where } \mathcal{X} = f_\xi \circ g_\theta(\mathcal{Z}). \quad (8)$$

Here,  $\mathcal{O}$  is the observed multi-dimensional data,  $\mathcal{X}$  is the multi-dimensional data represented by the proposed DTR,  $\mathcal{M}$  is a binary mask tensor that sets the observed location to be ones and others be zeros,  $g(\cdot)$  is the deep latent generative module, and  $f_\xi(\cdot)$  is the deep transform module.

<sup>1</sup>If we start from the original tensor, we need to calculate the latent tensor via one transform and then go back to the original tensor via the inverse transform under the invertibility assumption. Here, we start from the latent tensor, which only needs to go back to the original tensor via one transform without the invertibility assumption.

Although the model (8) is highly non-convex and nonlinear, there are still numerous available methods that can solve it. Specifically, we consider using the popular gradient descent optimization algorithm in deep learning, i.e., the adaptive moment estimation (Adam) [37] algorithm, to effectively optimize  $\xi$  and  $\theta$ . Once the optimal  $\xi$  and  $\theta$  are obtained, the multi-dimensional data  $\mathcal{X}$  can be achieved by Eq. (4).

## V. EXPERIMENTS

In this section, we conduct a series of experiments to verify the effectiveness and superiority of the proposed DTR. We first introduce some experimental settings in Section V-A, and then present experimental results in Section V-B.

### A. Experimental Settings

**Compared Methods.** To comprehensively evaluate the effectiveness of DTR, we compare it with five classic multi-dimensional data recovery methods, i.e., TNN [16], TRLRF [38], FTNN [20], FCTN [39], and HLRTF [17]. These methods are all tensor decomposition-based methods. Note that TNN and HLRTF adopt shallow SVD and NMF to characterize the frontal slices of latent tensor, respectively. To ensure optimal performance, all parameters associated with the compared methods are carefully adjusted according to the suggestions provided by the respective authors in their articles.

**Implementation.** We employ two HSIs (i.e., *WDC*<sup>2</sup> and *Pavia*<sup>3</sup>), eleven MSIs<sup>4</sup> (i.e., *Beads, Cloth, Flowers, Cd, Beers, Feathers, Statue, Toys, Jelly, Painting, and Watercolors*), and two videos<sup>5</sup> (i.e., *Bird* and *Sunflower*) to test the performance of the proposed DTR. The sampling rates for both random and tube missing cases are set as  $SR = \{0.1, 0.2, 0.3\}$ . Before the experiment, the gray values of all datasets are normalized band-by-band into the interval  $[0, 1]$ . All experiments are performed on a PC equipped with two Intel(R) Xeon(R) Silver 4210R CPUs, two NVIDIA RTX 3090 GPUs, and 128GB RAM. The proposed DTR and HLRTF are implemented by using

<sup>2</sup>Available at <https://engineering.purdue.edu/biehl/MultiSpec/hyperspectral.html>

<sup>3</sup>Available at [https://www.ehu.es/ccwintco/index.php/Hyperspectral\\_Remote\\_Sensing\\_Scenes](https://www.ehu.es/ccwintco/index.php/Hyperspectral_Remote_Sensing_Scenes)

<sup>4</sup>Available at <http://www.cs.columbia.edu/CAVE/databases/multispectral/>

<sup>5</sup>Available at <http://trace.eas.asu.edu/yuv/>.



TABLE I: The quantitative results for multi-dimensional data recovery by different methods (random missing cases). The **best** and **second-best** values are highlighted.

Method		TNN [16]		TRLRF [38]		FTNN [20]		FCTN [39]		HLRTF [17]		DTR	
Data	Sampling rate	PSNR	SSIM	PSNR	SSIM	PSNR	SSIM	PSNR	SSIM	PSNR	SSIM	PSNR	SSIM
HSI WDC (256×256×191)	0.1	33.56	0.9176	25.86	0.6817	37.71	0.9634	38.72	0.9487	<u>40.88</u>	<u>0.9839</u>	<b>45.05</b>	<b>0.9932</b>
	0.2	38.20	0.9668	26.49	0.7134	<u>43.87</u>	0.9879	43.59	0.9893	43.54	<u>0.9906</u>	<b>47.08</b>	<b>0.9954</b>
	0.3	41.47	0.9827	28.72	0.7971	<u>47.60</u>	0.9938	44.72	0.9916	45.81	<u>0.9941</u>	<b>47.86</b>	<b>0.9959</b>
HSI Pavia (256×256×80)	0.1	32.70	0.8989	30.74	0.8439	38.00	0.9705	39.05	0.9692	<u>41.71</u>	<u>0.9845</u>	<b>45.87</b>	<b>0.9942</b>
	0.2	37.86	0.9610	32.05	0.8771	44.78	0.9921	46.74	0.9941	<u>46.75</u>	<u>0.9948</u>	<b>49.32</b>	<b>0.9968</b>
	0.3	41.57	0.9809	34.14	0.9170	48.80	0.9963	48.28	0.9958	<u>49.09</u>	<u>0.9968</u>	<b>50.22</b>	<b>0.9974</b>
MSI Beads (256×256×31)	0.1	23.41	0.6456	23.13	0.5738	25.36	0.7818	26.26	0.7101	<u>30.41</u>	<u>0.8983</u>	<b>33.38</b>	<b>0.9582</b>
	0.2	28.05	0.8330	26.63	0.7316	30.96	0.9196	31.84	0.8906	<u>36.88</u>	<u>0.9736</u>	<b>39.03</b>	<b>0.9872</b>
	0.3	31.82	0.9165	27.68	0.7742	35.17	0.9647	38.01	0.9671	<u>41.30</u>	<u>0.9905</u>	<b>43.89</b>	<b>0.9950</b>
MSI Cloth (256×256×31)	0.1	25.17	0.7853	24.34	0.7225	28.45	0.8995	27.39	0.8455	<u>31.54</u>	<u>0.9430</u>	<b>32.34</b>	<b>0.9643</b>
	0.2	29.73	0.9110	27.69	0.8473	33.54	0.9666	33.51	0.9569	<u>38.12</u>	<u>0.9861</u>	<b>39.76</b>	<b>0.9921</b>
	0.3	33.36	0.9577	28.72	0.8733	37.31	0.9855	36.72	0.9667	<u>42.56</u>	<u>0.9947</u>	<b>43.26</b>	<b>0.9957</b>
MSI Flowers (256×256×31)	0.1	31.94	0.7925	21.75	0.4215	35.96	0.8821	32.46	0.7666	<u>40.45</u>	<u>0.9362</u>	<b>40.81</b>	<b>0.9445</b>
	0.2	35.97	0.8660	26.01	0.5419	40.60	0.9230	38.85	0.8753	<u>44.96</u>	<u>0.9521</u>	<b>45.95</b>	<b>0.9698</b>
	0.3	38.66	0.8948	27.00	0.6326	43.53	0.9377	39.94	0.8922	<u>48.33</u>	<u>0.9714</u>	<b>48.34</b>	<b>0.9728</b>
MSI Cd (256×256×31)	0.1	30.01	0.9113	31.01	0.8662	31.40	<b>0.9657</b>	29.23	0.8713	<u>31.91</u>	0.9596	<b>33.95</b>	<u>0.9615</u>
	0.2	33.81	0.9537	34.35	0.9316	35.85	<b>0.9843</b>	36.58	0.9510	<u>36.55</u>	0.9836	<b>39.17</b>	<u>0.9839</u>
	0.3	36.93	0.9729	35.98	0.9491	<u>38.78</u>	<b>0.9901</b>	38.39	0.9640	38.61	0.9884	<b>41.46</b>	<u>0.9887</u>
MSI Beers (256×256×31)	0.1	37.88	0.9679	37.94	0.9650	41.54	0.9871	40.65	0.9702	<u>43.80</u>	<b>0.9890</b>	<b>43.83</b>	<u>0.9882</u>
	0.2	43.50	0.9902	40.75	0.9782	47.13	<u>0.9957</u>	44.84	0.9878	<u>47.93</u>	0.9948	<b>48.71</b>	<b>0.9958</b>
	0.3	47.48	0.9959	42.61	0.9841	50.58	<b>0.9979</b>	48.02	0.9946	<u>50.79</u>	0.9968	<b>50.82</b>	<u>0.9970</u>
MSI Feathers (256×256×31)	0.1	30.81	0.8622	29.57	0.7451	34.51	0.9482	33.37	0.8876	<u>38.51</u>	<u>0.9721</u>	<b>39.39</b>	<b>0.9771</b>
	0.2	35.52	0.9402	34.84	0.8995	39.62	0.9804	37.83	0.9426	<u>43.94</u>	<u>0.9892</u>	<b>44.12</b>	<b>0.9895</b>
	0.3	38.98	0.9692	35.20	0.9175	43.17	0.9896	38.95	0.9538	<b>47.58</b>	<b>0.9939</b>	<u>46.35</u>	<u>0.9902</u>
MSI Statue (256×256×31)	0.1	38.62	0.8764	27.86	0.5878	40.54	0.8911	35.40	0.8297	<b>44.57</b>	<u>0.9540</u>	<u>44.34</u>	<b>0.9746</b>
	0.2	41.75	0.9030	28.83	0.5992	43.65	0.9130	43.65	0.9188	<u>47.73</u>	<u>0.9649</u>	<b>48.81</b>	<b>0.9777</b>
	0.3	43.31	0.9115	30.53	0.6757	45.12	0.9200	44.51	0.9245	<u>49.59</u>	<u>0.9709</u>	<b>51.10</b>	<b>0.9825</b>
MSI Toys (256×256×31)	0.1	31.27	0.8857	29.00	0.7253	35.67	0.9558	35.87	0.9272	<u>37.90</u>	<u>0.9624</u>	<b>38.86</b>	<b>0.9700</b>
	0.2	36.22	0.9520	28.85	0.8235	41.12	0.9835	39.23	0.9577	<u>45.34</u>	<u>0.9894</u>	<b>45.89</b>	<b>0.9902</b>
	0.3	39.67	0.9748	36.36	0.9333	44.70	0.9908	40.30	0.9669	<b>47.80</b>	<b>0.9922</b>	<u>47.05</u>	<u>0.9912</u>
MSI Jelly (256×256×31)	0.1	27.40	0.7546	28.12	0.7211	<u>31.03</u>	0.8924	30.02	0.7924	30.41	0.8983	<b>34.89</b>	<b>0.9542</b>
	0.2	31.94	0.8850	30.61	0.8143	<u>36.56</u>	0.9650	31.78	0.8500	<u>36.88</u>	<u>0.9736</u>	<b>41.41</b>	<b>0.9868</b>
	0.3	35.35	0.9399	31.56	0.8451	40.28	0.9835	32.87	0.8780	<u>41.30</u>	<u>0.9905</u>	<b>43.82</b>	<b>0.9914</b>
MSI Painting (256×256×31)	0.1	34.18	0.8950	32.14	0.8544	36.49	0.9356	36.92	0.9235	<u>38.94</u>	<u>0.9558</u>	<b>39.92</b>	<b>0.9644</b>
	0.2	38.48	0.9531	33.38	0.9138	40.84	0.9718	39.04	0.9488	<u>43.96</u>	<u>0.9835</u>	<b>44.89</b>	<b>0.9847</b>
	0.3	41.88	0.9744	34.42	0.9333	44.33	0.9844	40.04	0.9569	<u>47.23</u>	<u>0.9911</u>	<b>47.90</b>	<b>0.9927</b>
MSI Watercolors (256×256×31)	0.1	31.49	0.9043	30.10	0.8890	34.90	0.9574	34.88	0.9458	<u>37.88</u>	<b>0.9730</b>	<b>38.20</b>	<u>0.9721</u>
	0.2	36.41	0.9652	34.08	0.9396	40.21	0.9859	37.04	0.9633	<u>43.11</u>	<u>0.9900</u>	<b>44.78</b>	<b>0.9925</b>
	0.3	39.88	0.9830	35.84	0.9552	43.79	0.9931	37.98	0.9700	<u>46.53</u>	<u>0.9948</u>	<b>46.78</b>	<b>0.9950</b>
Video Bird (288×352×3×10)	0.1	22.81	0.8097	20.83	0.7368	22.24	0.7680	24.57	0.8525	<u>25.06</u>	<u>0.8693</u>	<b>26.85</b>	<b>0.9315</b>
	0.2	26.38	0.9011	24.43	0.8583	26.49	0.9015	26.22	0.8924	<u>29.86</u>	<u>0.9422</u>	<b>31.84</b>	<b>0.9729</b>
	0.3	29.16	0.9419	27.01	0.9088	29.80	0.9503	27.11	0.9098	<u>33.55</u>	<u>0.9720</u>	<b>34.82</b>	<b>0.9846</b>
Video Sunflower (288×352×3×10)	0.1	21.49	0.8448	22.13	0.8529	20.22	0.8399	24.21	0.9103	<u>24.68</u>	<u>0.9380</u>	<b>26.13</b>	<b>0.9595</b>
	0.2	25.74	0.9451	23.83	0.8705	23.81	0.9187	26.57	0.9329	<u>27.37</u>	<u>0.9577</u>	<b>29.30</b>	<b>0.9807</b>
	0.3	28.21	0.9594	25.38	0.8767	26.42	0.9245	27.46	0.9390	<u>29.68</u>	<u>0.9708</u>	<b>32.18</b>	<b>0.9856</b>
Average	0.1	30.18	0.8501	27.63	0.7458	32.93	0.9092	32.60	0.8767	<u>35.91</u>	<u>0.9478</u>	<b>37.59</b>	<b>0.9672</b>
	0.2	34.64	0.9284	30.19	0.8227	37.94	0.9593	37.15	0.9368	<u>40.86</u>	<u>0.9777</u>	<b>42.67</b>	<b>0.9864</b>
	0.3	37.85	0.9570	32.08	0.8649	41.29	0.9735	38.89	0.9514	<u>43.98</u>	<u>0.9873</u>	<b>45.06</b>	<b>0.9904</b>

the Python and the PyTorch library with GPU calculation, and other comparison methods are implemented by MATLAB (R2018a) with CPU calculation. In our experiments,  $g_{\theta}(\cdot)$  is set as the U-Net,  $f_{\xi}(\cdot)$  is set as the FCN,  $\hat{n}_3$  value is set as the  $n_3$ , the layer number for both modules is set to 2, the Adam algorithm is adopted to train the model with learning rate 0.001, and the maximum iteration step for both HLRTF and the proposed DTR is set to 7000.

**Evaluation Metrics.** Two quantitative evaluation metrics peak-signal-to-noise-ratio (PSNR) and structural similarity (SSIM) are selected to evaluate the overall quality of the recovered results. In general, higher PSNR and SSIM values

indicate better results.

## B. Experimental Results

Tables I-II list the evaluation metrics of the recovered results by different methods under the random missing and tube missing cases, respectively. Especially, we highlight best and second-best results by bold and underline, respectively. From Tables I-II, we can observe that FTNN and FCTN perform well for random missing cases, while the TNN performs well for tube missing cases. The quantitative evaluation results of HLRTF are superior compared to TNN and FTNN for nearly all cases. The reason behind this is that the nonlinear

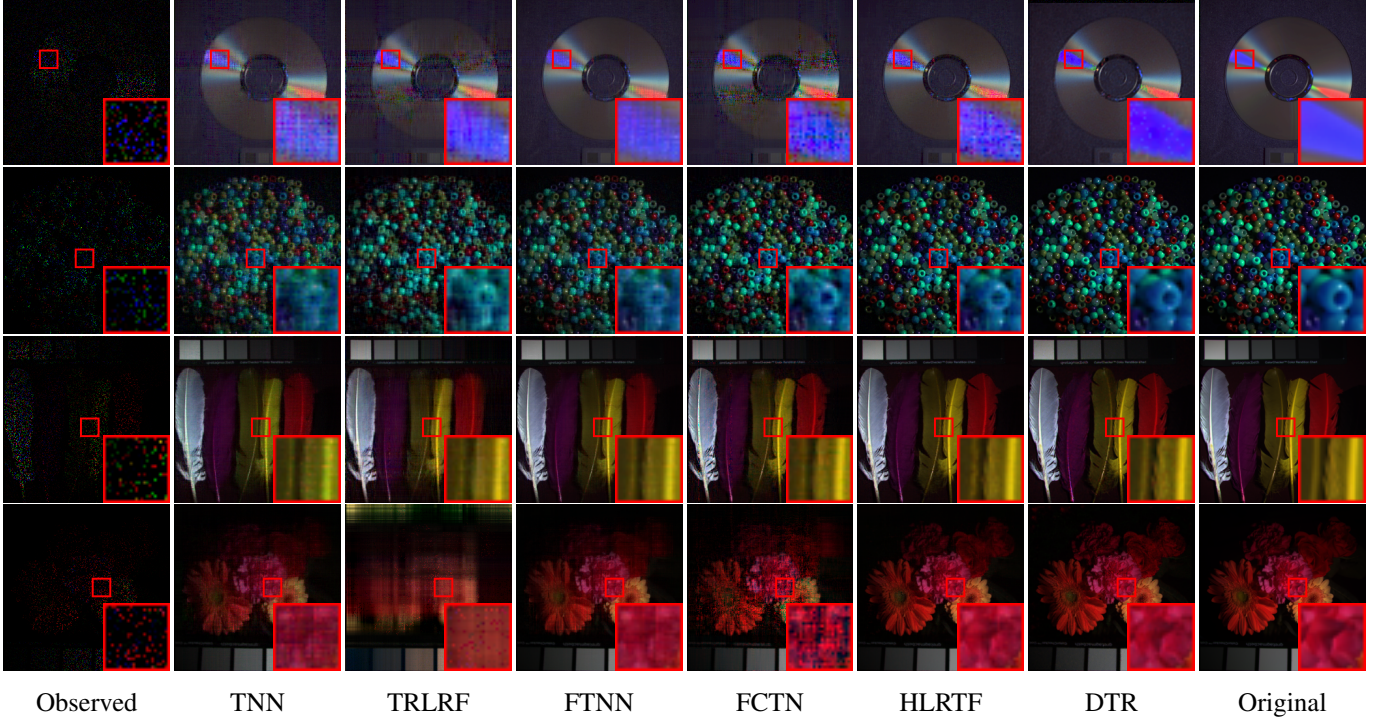


Fig. 3: The recovered pseudo-color images by different methods. From top to bottom: MSI *Cd* (R:10, G:20, B:30), *Beads* (R:10, G:20, B:30), *Feathers* (R:31, G:15, B:4), and *Flower* (R:31, G:15, B:4) with the random missing (SR = 0.1).

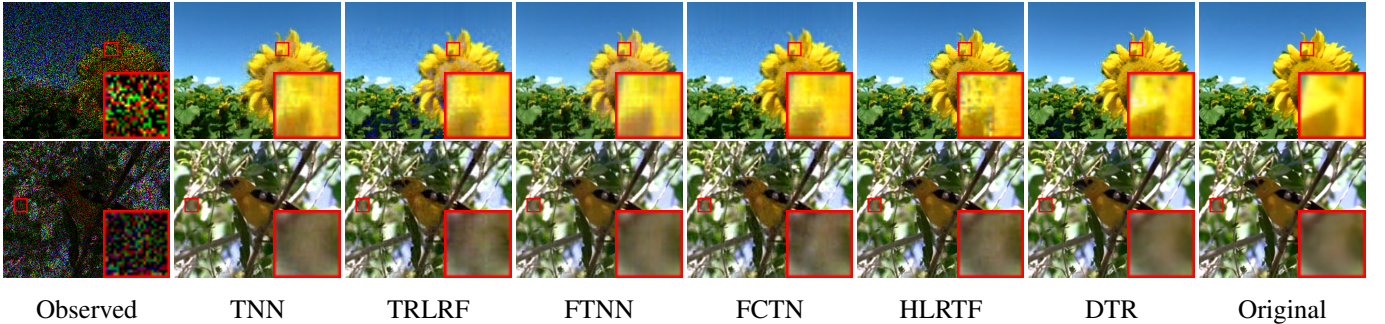


Fig. 4: The 10-th frame of the recovered results by all comparative methods on videos *Sunflower* and *Bird* with the random missing (SR = 0.3).

transform in HLRTF obtained by learning a multi-layer neural network can better capture the frontal slice relationships of multi-dimensional data. Additionally, it is worth noting that DTR significantly outperforms HLRTF<sup>6</sup> for most cases, which can be attributed to the powerful characterization ability of deep latent generator in contrast to shallow matrix factorization.

To visually compare the recovered results, we present visual illustrations of the recovered results obtained by different methods in Figs. 3-6. Aiming at a better visual comparison, we mark one local area and enlarge it under each image. From Figs. 3-6, we can observe that all the compared methods can somewhat recover the multi-dimensional data. The results of TNN and TRLRF contain some spatial blurring effects on

<sup>6</sup>Due to the additional TV regularization term existing in HLRTF, some recovered results of HLRTF are better than DTR.

MSIs (e.g., *Cd* and *Beads*). Although the FTNN and FCTN have better recovery effects than TNN and TRLRF visually, there are still some unsatisfactory performance in local details. The results of HLRTF have more spatial edges or textures compared to FTNN and FCTN, but small blurring effects still can be found. On the contrary, the proposed DTR performs better on the preservation of global structure and local details compared with the comparative methods.

Overall, the proposed DTR achieves superior performance on multi-dimensional data, including HSIs, MSIs, and videos. The superior performance of DTR can be attributed to the powerful representation ability of deep latent generative module and deep transform module. These two indispensable components allow DTR to more faithfully capture the rich textures and details in multi-dimensional data, which is particularly beneficial for

TABLE II: The quantitative results for multi-dimensional data recovery by different methods (tube missing cases). The **best** and **second-best** values are highlighted.

Method		TNN [16]		TRLRF [38]		FTNN [20]		FCTN [39]		HLRTF [17]		DTR	
Data	Sampling rate	PSNR	SSIM	PSNR	SSIM	PSNR	SSIM	PSNR	SSIM	PSNR	SSIM	PSNR	SSIM
HSI WDC (256×256×191)	0.1	20.55	0.3704	19.35	0.3302	20.62	0.4144	19.16	0.3530	<b>22.15</b>	<b>0.4993</b>	21.97	0.4905
	0.2	22.48	0.5003	21.79	0.4922	22.99	0.5521	21.78	0.4933	24.05	0.6011	<b>24.26</b>	<b>0.6244</b>
	0.3	24.17	0.6035	22.66	0.5554	24.82	0.6544	22.63	0.5557	<u>25.79</u>	<u>0.6916</u>	<b>26.15</b>	<b>0.7265</b>
HSI Pavia (256×256×80)	0.1	21.01	0.3334	19.31	0.2798	20.73	0.3679	19.50	0.3212	<u>22.60</u>	<u>0.4791</u>	<b>24.83</b>	<b>0.6417</b>
	0.2	22.94	0.4614	21.68	0.4263	23.31	0.5101	22.32	0.4595	<u>24.39</u>	<u>0.5737</u>	<b>27.48</b>	<b>0.7696</b>
	0.3	24.56	0.5777	23.14	0.5262	25.11	0.6281	23.13	0.5259	<u>26.23</u>	<u>0.6860</u>	<b>29.99</b>	<b>0.8595</b>
MSI Beads (256×256×31)	0.1	17.34	0.2868	16.29	0.2440	17.52	0.3712	15.35	0.2571	<u>19.16</u>	<u>0.4555</u>	<b>20.61</b>	<b>0.6226</b>
	0.2	19.27	0.4248	18.02	0.3674	20.12	0.5281	18.22	0.3787	<u>21.77</u>	<u>0.6242</u>	<b>23.72</b>	<b>0.7696</b>
	0.3	21.28	0.5501	18.90	0.4376	22.38	<u>0.6573</u>	19.05	0.4512	<u>23.03</u>	<u>0.6549</u>	<b>26.78</b>	<b>0.8728</b>
MSI Cloth (256×256×31)	0.1	18.27	0.3961	17.00	0.3510	18.18	0.4428	15.72	0.3456	<b>19.85</b>	<u>0.5025</u>	<u>19.40</u>	<b>0.5148</b>
	0.2	19.84	0.4967	19.37	0.4885	20.05	0.5366	19.45	0.4880	<u>21.01</u>	<u>0.5737</u>	<b>21.51</b>	<b>0.6795</b>
	0.3	21.37	0.5917	20.42	0.5559	21.75	0.6287	20.44	0.5567	<u>22.76</u>	<u>0.6704</u>	<b>23.77</b>	<b>0.7848</b>
MSI Flower (256×256×31)	0.1	24.75	0.5999	21.34	0.3660	21.51	0.6358	23.45	0.5638	<u>27.78</u>	<u>0.7611</u>	<b>29.36</b>	<b>0.8155</b>
	0.2	27.95	0.6943	24.93	0.5120	27.93	0.7510	26.62	0.6399	<u>31.25</u>	<u>0.8473</u>	<b>32.49</b>	<b>0.8993</b>
	0.3	30.49	0.7686	25.53	0.5359	31.06	0.8233	27.57	0.6710	<u>33.63</u>	<u>0.9005</u>	<b>35.33</b>	<b>0.9182</b>
MSI Cd (256×256×31)	0.1	24.84	0.7900	21.12	0.5117	22.00	0.8092	22.55	0.6321	<u>26.77</u>	<u>0.8888</u>	<b>29.26</b>	<b>0.8622</b>
	0.2	28.35	0.8776	24.57	0.7237	27.81	0.9060	25.07	0.7772	<u>30.62</u>	<u>0.9383</u>	<b>33.64</b>	<u>0.9321</u>
	0.3	31.40	0.9214	25.52	0.7372	31.83	0.9462	25.79	0.7584	<u>33.86</u>	<u>0.9595</u>	<b>36.94</b>	<b>0.9617</b>
MSI Beers (256×256×31)	0.1	25.43	0.8002	22.62	0.6764	18.03	0.5032	20.05	0.6876	<u>29.34</u>	<u>0.8965</u>	<b>30.65</b>	<b>0.8846</b>
	0.2	31.29	0.9171	25.77	0.7864	25.94	0.8348	26.75	0.8202	<u>35.24</u>	<u>0.9647</u>	<b>35.54</b>	<u>0.9552</u>
	0.3	35.09	0.9569	26.69	0.8010	34.09	0.9561	27.60	0.8290	<u>38.41</u>	<u>0.9782</u>	<b>39.74</b>	<b>0.9783</b>
MSI Feathers (256×256×31)	0.1	21.99	0.6267	18.59	0.3422	18.06	0.6411	17.57	0.4196	<u>23.88</u>	<b>0.7711</b>	<b>24.60</b>	<u>0.7436</u>
	0.2	24.89	0.7375	22.30	0.5276	21.97	0.7459	22.76	0.5688	<u>26.74</u>	<u>0.8415</u>	<b>27.88</b>	<b>0.8722</b>
	0.3	27.07	0.8066	23.49	0.5808	26.44	0.8349	23.80	0.6210	<u>29.61</u>	<u>0.8979</u>	<b>31.61</b>	<b>0.9272</b>
MSI Statue (256×256×31)	0.1	30.60	0.7611	18.14	0.1772	24.75	0.7420	27.23	0.6849	<b>33.26</b>	<u>0.8527</u>	<u>32.43</u>	<b>0.8853</b>
	0.2	34.70	0.8310	22.99	0.4487	34.45	0.8397	31.41	0.7692	<u>36.85</u>	<u>0.9158</u>	<b>36.15</b>	<b>0.9383</b>
	0.3	36.20	0.8565	24.73	0.4876	36.63	0.8672	34.14	0.7918	<b>38.21</b>	<u>0.9305</u>	<u>38.05</u>	<b>0.9400</b>
MSI Toys (256×256×31)	0.1	20.97	0.5969	20.23	0.4483	15.35	0.5736	18.15	0.5268	<u>23.33</u>	<u>0.7469</u>	<b>24.36</b>	<b>0.7532</b>
	0.2	24.13	0.7139	21.89	0.5281	20.82	0.7020	23.05	0.6645	<u>26.86</u>	<u>0.8403</u>	<b>27.95</b>	<b>0.8706</b>
	0.3	26.75	0.7947	24.12	0.6930	25.27	0.8009	24.33	0.7127	<u>29.54</u>	<u>0.8890</u>	<b>30.02</b>	<b>0.9071</b>
MSI Jelly (256×256×31)	0.1	17.18	0.2835	14.85	0.1794	16.35	0.3747	13.70	0.1883	<u>19.29</u>	<u>0.4574</u>	<b>22.53</b>	<b>0.6810</b>
	0.2	19.60	0.4090	17.86	0.3293	18.91	0.4848	17.81	0.3295	<u>22.05</u>	<u>0.5953</u>	<b>25.11</b>	<b>0.8052</b>
	0.3	21.78	0.5421	18.96	0.4073	21.23	0.6017	18.97	0.4044	<u>24.92</u>	<u>0.7360</u>	<b>27.64</b>	<b>0.8752</b>
MSI Painting (256×256×31)	0.1	25.19	0.6451	21.57	0.3818	21.71	0.6280	23.11	0.6029	<u>27.62</u>	<u>0.7580</u>	<b>29.35</b>	<b>0.7692</b>
	0.2	28.19	0.7584	25.36	0.5776	26.51	0.7543	26.53	0.6827	<u>30.82</u>	<b>0.8389</b>	<b>30.98</b>	<u>0.8297</u>
	0.3	30.81	0.8265	27.40	0.7008	30.32	0.8367	27.29	0.7098	<u>32.91</u>	<u>0.8840</u>	<b>33.82</b>	<b>0.8858</b>
MSI Watercolors (256×256×31)	0.1	22.51	0.5889	20.70	0.4980	16.35	0.4059	19.35	0.5236	<b>24.41</b>	<b>0.7097</b>	<u>24.11</u>	<u>0.6742</u>
	0.2	24.74	0.7027	23.60	0.6551	21.91	0.5966	23.64	0.6577	<u>26.92</u>	<u>0.8060</u>	<b>27.34</b>	<b>0.8131</b>
	0.3	26.58	0.7819	24.61	0.7015	25.41	0.7466	24.66	0.7062	<u>28.90</u>	<u>0.8649</u>	<b>30.16</b>	<b>0.8841</b>
Video Bird (288×352×3×10)	0.1	13.55	0.2178	12.78	0.3104	12.15	0.4171	13.10	0.3302	<u>16.21</u>	<u>0.6401</u>	<b>22.30</b>	<b>0.8523</b>
	0.2	17.14	0.6250	14.60	0.4381	16.46	0.6271	14.59	0.4305	<u>20.84</u>	<u>0.7976</u>	<b>26.81</b>	<b>0.9337</b>
	0.3	20.26	0.7640	19.01	0.6756	20.28	0.7810	15.42	0.4962	<u>24.17</u>	<u>0.8751</u>	<b>31.09</b>	<b>0.9702</b>
Video Sunflower (288×352×3×10)	0.1	17.41	0.7897	14.75	0.6046	16.72	0.7683	16.78	0.7410	<u>20.27</u>	<u>0.8744</u>	<b>23.39</b>	<b>0.9353</b>
	0.2	20.71	0.8823	17.79	0.7970	20.18	0.8667	17.62	0.7654	<u>24.20</u>	<u>0.9577</u>	<b>26.83</b>	<b>0.9647</b>
	0.3	23.40	0.9248	21.66	0.8796	22.78	0.9140	18.22	0.7990	<u>26.70</u>	<u>0.9582</u>	<b>29.57</b>	<b>0.9776</b>
Average	0.1	21.44	0.5391	18.58	0.3800	18.67	0.5397	18.98	0.4785	<u>23.73</u>	<u>0.6862</u>	<b>25.28</b>	<b>0.7417</b>
	0.2	24.41	0.6688	21.50	0.5399	23.29	0.6824	22.51	0.5950	<u>26.91</u>	<u>0.7811</u>	<b>28.51</b>	<b>0.8438</b>
	0.3	26.75	0.7511	23.12	0.6184	26.63	0.7785	23.54	0.6393	<u>29.24</u>	<u>0.8384</u>	<b>31.38</b>	<b>0.8979</b>

multi-dimensional data recovery tasks.

## VI. DISCUSSIONS

Two indispensable components (i.e., the deep latent generative module and the deep transform module) in the proposed DTR framework complement to each other and work together to make up a unified framework. In this section, we discuss the roles of each component in the DTR framework.

### A. The Contribution of Deep Latent Generative Module $g_{\theta}(\cdot)$

1) *Deep Latent Generator vs Shallow Matrix Factorization*: To verify the characterization ability of deep latent

generator, we compare the recovered results by the shallow characterization-based method (i.e., based on NMF) and deep characterization-based methods (i.e., based on deep latent generators). Table III shows the quantitative comparison of the proposed DTR variants with different latent tensor characterizations for HSI *Pavia*. We can observe that the recovered results of shallow characterization-based method are generally inferior to that of deep characterization-based methods, and the number of network parameters is much larger. It is rational to say that the deep latent generator is more effective and efficient than shallow matrix factorization.



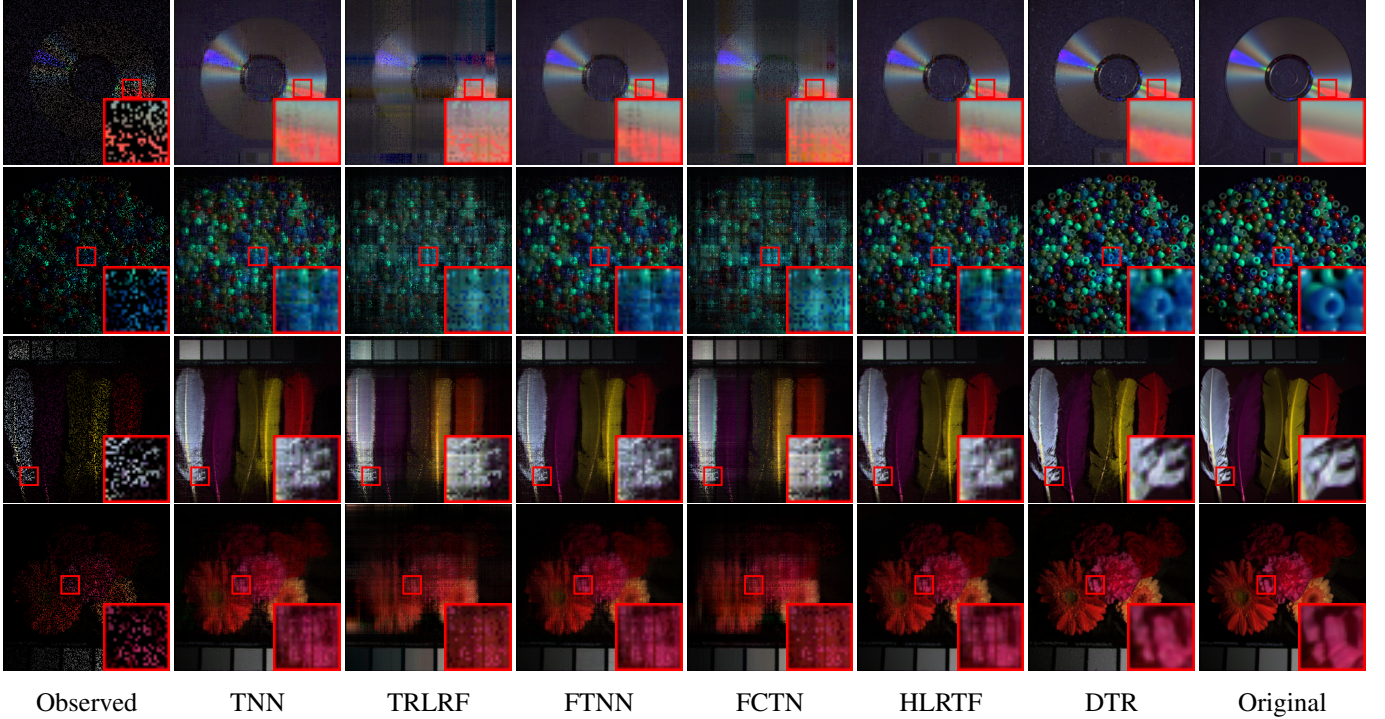


Fig. 5: The recovered pseudo-color images by different methods. From top to bottom: MSI *Cd* (R:10, G:20, B:30), *Beads* (R:10, G:20, B:30), *Feathers* (R:31, G:15, B:4), and *Flowers* (R:31, G:15, B:4) with the tube missing (SR = 0.3).

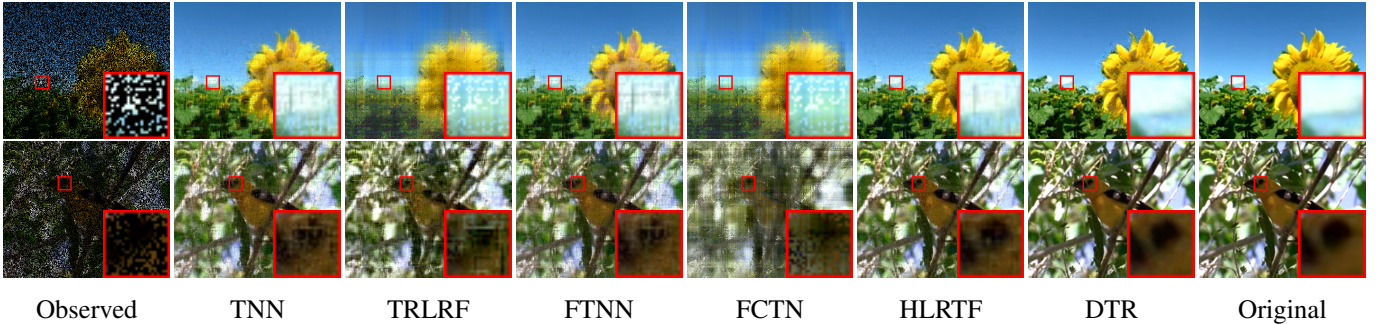


Fig. 6: The 10-th frame of the recovered results by all comparative methods on videos *Sunflower* and *Bird* with the tube missing (SR = 0.3).

TABLE III: Quantitative comparison of the proposed DTR variants with different latent tensor characterizations for HSI *Pavia* (random missing cases).

Sampling rate		0.1		0.2		0.3		Params (M)
		PSNR	SSIM	PSNR	SSIM	PSNR	SSIM	
Shallow	NMF	41.71	0.9845	46.75	0.9948	49.09	0.9968	2.102
	V-Net	43.09	0.9880	44.79	0.9918	45.95	0.9933	0.165
Deep	DenseNet	43.20	0.9881	48.80	0.9963	49.71	0.9971	0.659
	U-Net	45.87	0.9942	48.85	0.9966	50.22	0.9974	0.565
	U-Net-3D	<b>46.32</b>	<b>0.9945</b>	<b>49.33</b>	<b>0.9969</b>	<b>50.40</b>	<b>0.9975</b>	1.388

2) *The Influence of Different Networks*: Deep latent generative module plays a paramount role in the proposed DTR. We compare the recovered results by the proposed DTR with three

classic networks, i.e., V-Net [40], DenseNet [41], and U-Net [42]. Table III shows the quantitative comparison of different DTR variants for HSI *Pavia*, where “U-Net-3D” denotes the U-Net using 3D filters. We can observe that U-Net achieves better results compared to V-Net and DenseNet, which indicates that the U-Net may be a good choice for generating the latent tensor. In addition, while U-Net-3D achieves better recovery results compared to U-Net, it comes with nearly double number of parameters as U-Net. Considering the trade-off between efficiency and performance, we set the  $g_{\theta}(\cdot)$  as U-Net in our experiments.

3) *The Influence of the Layer Number of  $g_{\theta}(\cdot)$* : The layer number of deep latent generative module  $g_{\theta}(\cdot)$  is a crucial parameter that determines the characterization ability of  $g_{\theta}(\cdot)$ . Table IV presents the quantitative comparison of the proposed

DTR with different layer number  $L$  of  $g_\theta(\cdot)$  for HSI *Pavia*. As shown in Table IV, we can observe that increasing  $L$  enhances the performance when  $L$  is small. However, when  $L$  becomes larger, the results are not as desirable as expected. This is because a deeper network is more likely to suffer from the vanishing gradient. In our experiments, we set the layer number  $L$  of  $g_\theta(\cdot)$  to 2 to strike a balance between performance and the risk of vanishing gradient.

TABLE IV: Quantitative comparison of the proposed DTR with different layer number (i.e.,  $L$  and  $K$ ) of  $g_\theta(\cdot)$  and  $f_\xi(\cdot)$  for HSI *Pavia* (random missing cases).

Sampling rate	0.1		0.2		0.3		Params (M)	
	PSNR	SSIM	PSNR	SSIM	PSNR	SSIM		
$g_\theta(\cdot)$	$L = 1$	37.13	0.9555	39.27	0.9708	39.78	0.9743	0.095
	$L = 2$	45.87	<b>0.9942</b>	<b>49.32</b>	<b>0.9968</b>	<b>50.22</b>	<b>0.9974</b>	0.565
	$L = 3$	<b>46.19</b>	<b>0.9942</b>	47.86	0.9958	49.58	0.9970	2.412
	$L = 4$	45.34	0.9935	48.28	0.9963	49.08	0.9968	9.821
	$L = 5$	45.28	0.9933	48.39	0.9962	49.04	0.9968	103.423
$f_\xi(\cdot)$	$K = 1$	45.10	0.9929	48.97	0.9967	49.79	0.9973	0.559
	$K = 2$	<b>45.87</b>	<b>0.9942</b>	<b>49.32</b>	<b>0.9968</b>	<b>50.22</b>	<b>0.9974</b>	0.565
	$K = 3$	45.49	0.9940	48.73	0.9965	49.81	0.9973	0.572
	$K = 4$	45.75	0.9939	48.66	0.9965	50.09	0.9973	0.578
	$K = 5$	45.46	0.9939	48.55	0.9965	49.54	0.9972	0.584
DTR Without $f_\xi(\cdot)$	44.36	0.9923	48.24	0.9961	49.74	0.9971	0.552	

4) *The Influence of  $\hat{n}_3$  Value:* To analyze the influence of  $\hat{n}_3$  value on recovery effects of the proposed DTR, we conduct quantitative comparison of the proposed DTR with different  $\hat{n}_3$  value for HSI *Pavia* in Table V. As shown in Table V, we can observe that a moderate  $\hat{n}_3$  can obtain a satisfactory recovery effects. To balance the performance of the proposed DTR and the computational complexity, we set  $\hat{n}_3 = n_3$  in all our experiments.

TABLE V: Quantitative comparison of the proposed DTR with different  $\hat{n}_3$  value for HSI *Pavia* (random missing cases).

Sampling rate	0.1		0.2		0.3		Params (M)
	PSNR	SSIM	PSNR	SSIM	PSNR	SSIM	
$\hat{n}_3 = n_3/4$	44.95	0.9931	47.19	0.9956	49.02	0.9967	0.531
$\hat{n}_3 = n_3/2$	44.99	0.9933	48.60	0.9964	50.27	0.9974	0.542
$\hat{n}_3 = n_3$	<b>45.87</b>	<b>0.9942</b>	<b>49.32</b>	<b>0.9968</b>	50.22	0.9974	0.565
$\hat{n}_3 = 2n_3$	45.72	0.9941	48.97	<b>0.9968</b>	<b>50.40</b>	<b>0.9975</b>	0.611

### B. The Contribution of Deep Transform Module $f_\xi(\cdot)$

The deep transform module  $f_\xi(\cdot)$  is another indispensable component in the proposed DTR. Table IV presents the quantitative comparison of the proposed DTR with different the layer number  $K$  of  $f_\xi(\cdot)$  for HSI *Pavia*. It can be observed that using the deep transform module can achieve better recovered results, which reflects the effectiveness of deep transform module. Particularly, when  $K = 1$ ,  $f_\xi(\cdot)$  degenerates into a linear transform. We can observe that nonlinear transform (i.e.,  $K \geq 2$ ) can achieve better recovered results, which indicates that nonlinear transform can better capture the frontal slice relationships of multi-dimensional data. Similar to the deep latent generative module, we can observe that increasing  $K$  enhances the performance when  $K$  is small. However, when  $K$  becomes larger, the performance tends to drop. Thus, in our experiments, we set the layer number  $K$  of  $f_\xi(\cdot)$  to 2.

## VII. CONCLUSION

In this paper, we proposed a unified deep tensor representation (termed as DTR) framework by synergistically combining the deep latent generative module and the deep transform module. The new DTR framework not only allows us to better understand the classic shallow representations, but also leads us to explore new representation. Extensive experiments demonstrate that the proposed DTR can achieve satisfactory performance on multi-dimensional data recovery problems.

## REFERENCES

- [1] C. Huang, M. K. Ng, T. Wu, and T. Zeng, "Quaternion-based dictionary learning and saturation-value total variation regularization for color image restoration," *IEEE Transactions on Multimedia*, vol. 24, pp. 3769–3781, 2022.
- [2] Y. Liu, Z. Long, and C. Zhu, "Image completion using low tensor tree rank and total variation minimization," *IEEE Transactions on Multimedia*, vol. 21, no. 2, pp. 338–350, 2019.
- [3] F. Fang, T. Wang, Y. Wang, T. Zeng, and G. Zhang, "Variational single image dehazing for enhanced visualization," *IEEE Transactions on Multimedia*, vol. 22, no. 10, pp. 2537–2550, 2020.
- [4] A. Anandkumar, R. Ge, D. Hsu, S. M. Kakade, and M. Telgarsky, "Tensor decompositions for learning latent variable models," *Journal of Machine Learning Research*, vol. 15, pp. 2773–2832, 2014.
- [5] S. Gandy, B. Recht, and I. Yamada, "Tensor completion and low-n-rank tensor recovery via convex optimization," *Inverse problems*, vol. 27, no. 2, p. 025010, 2011.
- [6] Z. Fabian, R. Heckel, and M. Soltanolkotabi, "Data augmentation for deep learning based accelerated MRI reconstruction with limited data," in *International Conference on Machine Learning*, 2021, pp. 3057–3067.
- [7] X. Li, Y. Ye, and X. Xu, "Low-rank tensor completion with total variation for visual data inpainting," in *Proceedings of the AAAI Conference on Artificial Intelligence*, vol. 31, 2017, pp. 2210–2216.
- [8] J. Tian, Z. Han, W. Ren, X. Chen, and Y. Tang, "Snowflake removal for videos via global and local low-rank decomposition," *IEEE Transactions on Multimedia*, vol. 20, no. 10, pp. 2659–2669, 2018.
- [9] J. You, X. Li, M. Low, D. Lobell, and S. Ermon, "Deep gaussian process for crop yield prediction based on remote sensing data," in *Proceedings of the AAAI Conference on Artificial Intelligence*, vol. 31, 2017, pp. 4559–4566.
- [10] H. Li, R. Feng, L. Wang, Y. Zhong, and L. Zhang, "Superpixel-based reweighted low-rank and total variation sparse unmixing for hyperspectral remote sensing imagery," *IEEE Transactions on Geoscience and Remote Sensing*, vol. 59, no. 1, pp. 629–647, 2021.
- [11] H. Zeng, J. Xue, H. Q. Luong, and W. Philips, "Multimodal core tensor factorization and its applications to low-rank tensor completion," *IEEE Transactions on Multimedia*, pp. 1–15, 2022.
- [12] M. Lv, W. Li, T. Chen, J. Zhou, and R. Tao, "Discriminant tensor-based manifold embedding for medical hyperspectral imagery," *IEEE Journal of Biomedical and Health Informatics*, vol. 25, no. 9, pp. 3517–3528, 2021.
- [13] H. Chen and J. Li, "Neural tensor model for learning multi-aspect factors in recommender systems," in *International Joint Conference on Artificial Intelligence*, 2020, pp. 2449–2455.
- [14] Z. Chen, Z. Xu, and D. Wang, "Deep transfer tensor decomposition with orthogonal constraint for recommender systems," in *Proceedings of the AAAI Conference on Artificial Intelligence*, vol. 35, 2021, pp. 4010–4018.
- [15] Z. Chen, J. Yao, G. Xiao, and S. Wang, "Efficient and differentiable low-rank matrix completion with back propagation," *IEEE Transactions on Multimedia*, vol. 25, pp. 228–242, 2023.
- [16] Z. Zhang, G. Ely, S. Aeron, N. Hao, and M. Kilmer, "Novel methods for multilinear data completion and de-noising based on Tensor-SVD," in *Proceedings of the IEEE Conference on Computer Vision and Pattern Recognition*, 2014, pp. 3842–3849.
- [17] Y.-S. Luo, X.-L. Zhao, D.-Y. Meng, and T.-X. Jiang, "HLRTF: Hierarchical low-rank tensor factorization for inverse problems in multi-dimensional imaging," in *Proceedings of the IEEE Conference on Computer Vision and Pattern Recognition*, 2022, pp. 19 281–19 290.
- [18] X.-L. Zhao, W.-H. Xu, T.-X. Jiang, Y. Wang, and M. K. Ng, "Deep plug-and-play prior for low-rank tensor completion," *Neurocomputing*, vol. 400, pp. 137–149, 2020.



- [19] T.-X. Jiang, T.-Z. Huang, X.-L. Zhao, and L.-J. Deng, "Multi-dimensional imaging data recovery via minimizing the partial sum of tubal nuclear norm," *Journal of Computational and Applied Mathematics*, vol. 372, p. 112680, 2020.
- [20] T.-X. Jiang, M. K. Ng, X.-L. Zhao, and T.-Z. Huang, "Framelet representation of tensor nuclear norm for third-order tensor completion," *IEEE Transactions on Image Processing*, vol. 29, pp. 7233–7244, 2020.
- [21] C. Lu, X. Peng, and Y. Wei, "Low-rank tensor completion with a new tensor nuclear norm induced by invertible linear transforms," in *Proceedings of the IEEE Conference on Computer Vision and Pattern Recognition*, 2019, pp. 5989–5997.
- [22] B. Madathil and S. N. George, "DCT based weighted adaptive multi-linear data completion and denoising," *Neurocomputing*, vol. 318, pp. 120–136, 2018.
- [23] M. E. Kilmer and C. D. Martin, "Factorization strategies for third-order tensors," *Linear Algebra and Its Applications*, vol. 435, no. 3, pp. 641–658, 2011.
- [24] P. Zhou, C. Lu, Z. Lin, and C. Zhang, "Tensor factorization for low-rank tensor completion," *IEEE Transactions on Image Processing*, vol. 27, no. 3, pp. 1152–1163, 2018.
- [25] F. Wu, Y. Li, C. Li, and Y. Wu, "A fast tensor completion method based on tensor QR decomposition and tensor nuclear norm minimization," *IEEE Transactions on Computational Imaging*, vol. 7, pp. 1267–1277, 2021.
- [26] C. Lu, J. Feng, Y. Chen, W. Liu, Z. Lin, and S. Yan, "Tensor robust principal component analysis with a new tensor nuclear norm," *IEEE Transactions on Pattern Analysis and Machine Intelligence*, vol. 42, no. 4, pp. 925–938, 2020.
- [27] M. K. Ng, X. Zhang, and X.-L. Zhao, "Patched-tube unitary transform for robust tensor completion," *Pattern Recognition*, vol. 100, p. 107181, 2020.
- [28] G. Song, M. K. Ng, and X. Zhang, "Robust tensor completion using transformed tensor singular value decomposition," *Numerical Linear Algebra with Applications*, vol. 27, no. 3, p. e2299, 2020.
- [29] T.-X. Jiang, X.-L. Zhao, H. Zhang, and M. K. Ng, "Dictionary learning with low-rank coding coefficients for tensor completion," *IEEE Transactions on Neural Networks and Learning Systems*, vol. 34, no. 2, pp. 932–946, 2023.
- [30] H. Kong, C. Lu, and Z. Lin, "Tensor Q-rank: new data dependent definition of tensor rank," *Machine Learning*, vol. 110, no. 7, pp. 1867–1900, 2021.
- [31] Y. Zheng and A.-B. Xu, "Tensor completion via tensor QR decomposition and  $L_{2,1}$ -norm minimization," *Signal Processing*, vol. 189, p. 108240, 2021.
- [32] M. E. Kilmer, K. Braman, N. Hao, and R. C. Hoover, "Third-order tensors as operators on matrices: A theoretical and computational framework with applications in imaging," *SIAM Journal on Matrix Analysis and Applications*, vol. 34, no. 1, pp. 148–172, 2013.
- [33] T. G. Kolda and B. W. Bader, "Tensor decompositions and applications," *SIAM Review*, vol. 51, no. 3, pp. 455–500, 2009.
- [34] Y.-S. Luo, X.-L. Zhao, T.-X. Jiang, Y. Chang, M. K. Ng, and C. Li, "Self-supervised nonlinear transform-based tensor nuclear norm for multi-dimensional image recovery," *IEEE Transactions on Image Processing*, vol. 31, pp. 3793–3808, 2022.
- [35] Z. Li, T. Sun, H. Wang, and B. Wang, "Adaptive and implicit regularization for matrix completion," *SIAM Journal on Imaging Sciences*, vol. 15, no. 4, pp. 2000–2022, 2022.
- [36] J. Fan and J. Cheng, "Matrix completion by deep matrix factorization," *Neural Networks*, vol. 98, pp. 34–41, 2018.
- [37] D. P. Kingma and J. Ba, "Adam: A method for stochastic optimization," in *International Conference on Learning Representations*, 2015.
- [38] L. Yuan, C. Li, D. Mandic, J. Cao, and Q. Zhao, "Tensor ring decomposition with rank minimization on latent space: An efficient approach for tensor completion," in *Proceedings of the AAAI Conference on Artificial Intelligence*, vol. 33, 2019, pp. 9151–9158.
- [39] Y.-B. Zheng, T.-Z. Huang, X.-L. Zhao, Q. Zhao, and T.-X. Jiang, "Fully-connected tensor network decomposition and its application to higher-order tensor completion," in *Proceedings of the AAAI Conference on Artificial Intelligence*, vol. 35, 2021, pp. 11 071–11 078.
- [40] F. Milletari, N. Navab, and S.-A. Ahmadi, "V-Net: Fully convolutional neural networks for volumetric medical image segmentation," in *2016 Fourth International Conference on 3D Vision*, 2016, pp. 565–571.
- [41] G. Huang, Z. Liu, L. van der Maaten, and K. Q. Weinberger, "Densely connected convolutional networks," in *Proceedings of the IEEE Conference on Computer Vision and Pattern Recognition*, 2017, pp. 2261–2269.
- [42] O. Ronneberger, P. Fischer, and T. Brox, "U-Net: Convolutional networks for biomedical image segmentation," in *Medical Image Computing and Computer-Assisted Intervention*, 2015, pp. 234–241.